LA-UR 86-1574

Los Alamos National Laboratory is operated by the University of California for the United States Department of Energy under contract W-7405-ENG-36.

TITLE: NEUTRON-INDUCED GAMMA-RAY SPECTROSCOPY: SIMULATIONS FOR CHEMICAL MAPPING OF PLANETARY SURFACES.

LA-UR--86-1574

DE86 011261

AUTHOR(S): J. Brückner, H, Wänke, and R. C. Reedy

SUBMITTED TO: Proceedings of the 17th Lunar and Planetary Science Conference.

DISCLAIMER

Los Alamos Los Alamos National Laboratory
Los Alamos, New Mexico 87545

FORM NO 836 R4
ST NO 2629 5/81

Neutron-Induced Gamma-Ray Spectroscopy: Simulations for Chemical Mapping of Planetary Surfaces.

J. Brückner and H. Wänke
Max-Planck-Institut für Chemie, Mainz

R. C. Reedy
Max-Planck-Institut für Chemie, Mainz, and Los Alamos National Laboratory

Short title: Simulations for Planetary Gamma-ray Spectroscopy.

submitted to: Proceedings of the 17th Lunar and Planetary Science Conference, Lunar and Planetary Institute, Houston
April 17, 1986

Abstract

Cosmic rays interact with the surface of a planetary body and produce a cascade of secondary particles, such as neutrons. Neutron-induced scattering and capture reactions play an important role in the production of discrete gamma-ray lines that can be measured by a gamma-ray spectrometer on board of an orbiting spacecraft. These data can be used to determine the concentration of many elements in the surface of a planetary body, which provides clues to its bulk composition and in turn to its origin and evolution. To investigate the gamma rays made by neutron interactions, thin targets were irradiated with neutrons having energies from 14 MeV to 0.025 eV. By means of foil activation technique the ratio of epithermal to thermal neutrons was determined to be similar to that in the Moon. Gamma rays emitted by the targets and the surrounding material were detected by a high-resolution germanium detector in the energy range of 0.1 to 8 MeV. Most of the gamma-ray lines that are expected to be used for planetary gamma-ray spectroscopy were found in the recorded spectra and the principal lines in these spectra are presented. The majority of gamma-ray lines are narrow without noticeable Doppler broadening except for the carbon inelastic line at 4.4 MeV that is very broad and therefore, of limited use for planetary analysis, and for five asymmetric germanium lines produced by the detector itself. Unfolding of the gamma-ray spectra, subtraction of background, and correcting for gamma-ray absorption were performed to determine the gamma-ray fluxes emitted by the target. Studies of several elements show how well the target signals could be extracted from the general background. Complex features in the

recorded gamma-ray spectra can be compared to what is expected from planetary measurements. Possible interfering background encountered during a planetary mission is briefly outlined.

Introduction

The exploration of the solar system made a big progress when man started to launch machines into space to fly to other planets and their satellites. The spacecrafts and their scientific instruments became more and more sophisticated leading to new observations of hitherto unknown worlds, but also to many new questions. Therefore, new missions to planetary bodies, as planets, satellites, asteroids, and comets, are planned. Comparative studies of planetary bodies will provide a better understanding of origin, evolution, and present state of the solar system including the Earth. In this context advanced remote sensing techniques will play an important role for gathering a large and precise data base.

Accretion and global differentiation with formation of core, mantle, and crust are foundamental processes during the evolution of a planetary body and its chemical composition is an important source of information. Reliable estimation of bulk composition of planetary bodies exist only for those of which we have samples for laboratory analysis [Wänke, 1981]. Besides direct samples from Earth and Moon, we have certain classes of meteorites that seem to originate from the same body: the Eucrites, Howardites, and Diogenites from the Eucrite Parent Asteroid [Dreibus and Wänke, 1980], the SNC-meteorites (Shergottites, Nakhlites, and Chassigny) from Mars [Becker and Pepin, 1984, Dreibus and Wänke, 1985], and Antarctic meteorites from the Moon [Palme et al., 1983, Ostertag et

al., 1985]. The identification of parent bodies of meteorites is only possible after a chemical analysis of parts of their surface. Basaltic rocks play a special role in this process because they represent partial melts of the underlying mantle and hence are probes for the chemical composition of mantle material that otherwise is not accessible [Basaltic Volcanism, 1981].

The determination of the chemical composition of a planetary surface can be carried out by sample-return mission, in-situ analysis, and by orbital remote sensing, each having specific advantages. The focus of this paper is on planetary (remote) gamma-ray spectroscopy that can provide data on the concentration of many elements on a global and local scale.

Mapping

For the best remote sensing, a spacecraft carrying a gamma-ray spectrometer (GRS) on board has to be in a low-altitude, circular polar orbit permitting the GRS to fly over the entire surface and to measure the energy spectrum of gamma rays emitted by the surface materials. Characteristic gamma radiation from a planetary surface is produced by the decay of natural radionuclides and by the interaction of cosmic-ray particles with the surface [Reedy et al., 1973]. Continuous recording of gamma-ray spectra from overflown terrain will permit the synthesis of surface spectra from the entire body, larger geological regions, and smaller areas. The chemical information contained in the spectra will allow us to map the variation of elemental concentrations on different scales [Arnold et al., 1977].

Spatial resolution and analytical precision improve as counting statistics improve, hence long-term data accumulation is required, e.g. NASA's planned Mars Observer will take data for two terrestrial years orbiting in an altitude of about 350 km [Planetary Exploration, 1983]. Gamma rays reaching an omnidirectional responding GRS travel different lengths inside the surface, short ones from the nadir area and longer ones from more distant areas. The gamma-ray attenuation produces a kind of collimation resulting in an effective detectable area below the GRS whose diameter is about equal to the GRS altitude [Reedy et al., 1973]. Improved spatial resolution is normally obtained at some sacrifice of analytical precision except at high latitudes where the coverage is better than at equatorial regions [Metzger et al., 1975]. If element abundances vary rapidly on the surface, deconvolution techniques can also improve the resolution [Metzger et al., 1977].

Cosmic rays

All bodies in the solar system including artificial objects are bombarded by cosmic-ray particles, provided they have a weak magnetic field and a thin atmosphere, only. These particles consist mainly of protons, about 10 % alpha particles, and about 1 % heavier nuclei. The galactic cosmic rays (GCR) that come from outside the solar system, have particle energies of 0.1 to 3 GeV/nucleon and higher and a low flux of about 3 particles/$cm^2 \cdot s$. The GCR flux is slightly modulated inside the heliosphere (about 50 AU away from the sun) [Reedy et al., 1983]. The solar cosmic rays (SCR), emitted irregulary by major flares on the sun, have energies

of 10-100 MeV/nucleon and a mean flux of about 100 particles per $cm^2 \cdot s$. For rare strong SCR events, the fluence of protons with energies above 10 MeV can range from 10^5 to 10^{11} protons/cm^2 over a few days, while there are essentially no SCR particles most of the time [Reedy et al., 1983], thus SCR-produced gamma rays are usualy unimportant for planetary gamma-ray spectroscopy [Reedy et al., 1973].

Secondary Particles

Energy, charge, and mass of a cosmic-ray particle and the chemical composition of the target matter mainly determine which interaction processes are dominant: ionization energy loss or nuclear reactions that lead to particle cascades, i.e. production of secondary particles, which again interact nonelastically to produce further particles, and so on. In such a cascade, part of the energy is lost by break-up of nuclei, nuclear excitation, evaporation and knock-on hadrons (neutrons, protons, pions, etc.).

The dominant strongly-interacting particles with energies below 100 MeV are neutrons because charged particles below 100 MeV are stopped by ionization energy loss. Most of the neutrons are produced by evaporation and have energies on the order of a few MeV, while less neutrons resulting from knock-on processes having energies up to 100 MeV [Reedy and Arnold, 1972].

In the lunar surface, about 10 neutrons per incident GCR-particle are produced [Reedy and Arnold, 1972]. Due to production, escape, and reactions of neutrons, equilibrium neutron spectra are produced that extent down to very low energies

[Lingenfelter et al., 1972, Kornblum et al., 1973]. The emitted flux of albedo neutrons depends on the composition of the surface because the macroscopic neutron cross section is determined by the concentration of major and minor elements and some trace elements with high cross sections. In addition, the neutron spectrum is altered due to the amount of water present in the surface [Lingenfelter et al., 1961]. The moderating effect of hydrogen influences the ratio of thermal to epithermal neutrons, which increases (nonlinearly) with the H concentration [Lapides, 1981]. The use of suitable neutron detectors will provide additional data on the variation of H in a planetary surface [Haines and Metzger, 1984a].

Gamma rays are produced not only by interaction of primary particles with matter, but predominantly by secondary cascade particles such as neutrons. Discrete gamma-ray lines that are indicative for a certain element can result from the following reactions: decay of proton and neutron induced radionuclides, proton spallation, nonelastic neutron scattering, and neutron capture. Scattering reactions excite a certain nuclear level, while capture of a neutron excites due to its binding energy (about 8 MeV). Deexcitation of the nucleus takes place via prompt emission of one or a cascade of gamma rays. The term prompt is used in contrast to beta-delayed gamma rays emitted by radioactive nuclei.

Depending on the type and energy of cosmic-ray particles the effective interaction length in silicious material varies from a few millimeters for SCR heavy nuclei to a few meters for GCR protons. The deep penetration of most GCR particles causes gamma-ray production over a great depth, but due to gamma-ray

attenuation the effective sampling depth is about 30 cm (assuming a density of 2 g/cm^3). This depth should be compared with other methods such as orbital x-ray, visible, or infrared spectroscopy, where only the uppermost micro- or millimeter of the surface can be investigated.

Lunar Spectra

The Moon was the target of an orbital gamma-ray exploration as part of the Apollo program. The detector of the lunar GRS consisted of a NaI(Tl) crystal [Harrington et al., 1974] that had the advantage of working without cooling but the disadvantage of a rather poor energy resolution. The lunar GRS provided data on the concentration of Th, K, Fe, Mg, and Ti. Due to the poor resolution of the NaI(Tl) detector, rather difficult unfolding methods had to be applied to the recorded gamma-ray spectra in order to generate element concentration maps [Arnold et al., 1977, Bielefeld et al., 1976, Davis, 1980, Metzger et al., 1977]. Therefore, detectors with a better energy resolution, such as Ge detectors, should be used for future missions [Metzger et al., 1975]. The hitherto main disadvantage of Ge(Li) detectors having to be kept cold all the time, has been overcome by the development of high-purity germanium (HPGe) detectors. These crystals can be stored at room temperatures prior and during the launch and also during the cruise phase, and only for data-taking they have to be cooled down to temperatures of about 120 K, which nowadays can be managed by means of a passive radiator (no liquid nitrogen required) [Bard et al., 1982].

Simulations

To investigate the gamma rays induced by GCR particle interaction with matter several approaches can be made. As a basic step we restricted ourself to secondary neutrons as being the most important members of the nuclear cascade for discrete gamma-ray production [Reedy, 1978]. Several thin targets were irradiated with neutrons having a spectrum ranging from 14 MeV down to thermal energies. Neutron-scattering and -capture induced reactions produced prompt gamma-rays that were accumulated by a high-resolution GRS [Brückner et al., 1984]. The experiment will demonstrate the good application of Ge detectors for anticipated planetary missions.

Experimental Procedure

The irradiation facility of the Max-Planck-Institute for Chemistry in Mainz, F.R. Germany, was used for the prompt gamma-ray experiments. The irradiation hall was divided into two parts by a 75 cm thick concrete shielding wall (Figure 1), in which a window with an opening of 75x100 cm was built. A 14-MeV sealed type neutron generator was located in the center of part A (size 3x3x3 m). The targets were placed 2 m away from the generator into the window near the side facing part B. There, a HPGe detector and shielding material was set up permitting a short target-detector distance of 20 cm.

The neutron generator emits isotropically neutrons via the T(d,n) reaction. The maximum source strength of $2 \cdot 10^{10}$ neutrons/s was just strong enough to activate monitor foils at the target position. During in-beam gamma-counting, the thermal neutron-flux

component was continuously monitored by a BF_3-counter and the source strength of the generator was adjusted to $7 \cdot 10^7$ neutrons/s so that the deadtime of the GRS didn't exceed a given level.

The energy distribution of the neutrons at the target position was controlled by the following conditions: i) 14-MeV neutrons emitted in a solid angle covering the target area could reach the target without interactions with matter, ii) 14-MeV neutrons emitted in other solid angles were moderated by multiple scattering in the surrounding walls and a certain percentage of them arrived at the target with reduced energy. Therefore, the generator and the walls acted as one extented neutron source producing a neutron spectrum from 14 MeV down to thermal energies (0.025 eV).

The inlay of Figure 1 shows the consecutive shielding layers of lead, boron, and paraffin around the Ge detector. Except at the front side, the detector was surrounded by 5 cm thick lead bricks in order to suppress the background gamma-radiation and to collimate its omnidirectional response. Because of radiation damage and of neutron-induced gamma-rays, the detector and the lead bricks were completely shielded by a 3 cm thick layer of boric acid granules enclosed in thin wooden plates. The outermost shielding consisted of 20 to 50 cm thick paraffin blocks, except for 5 cm thick ones at the front side. The big mass of paraffin prevented the fast neutrons from entering room B through the window, while thermal neutrons could reach room B and did induce background gamma radiation. However, fast neutrons could penetrate the necessary thin front shielding of the detector and gave rise to radiation damage of the Ge crystal. The overall effect of the shielding was an improvement of the signal to noise ratio of the target gamma rays.

The detector consisted of a high-purity, coaxial germanium crystal having an active volume of 92 cm^3 with an efficiency of 18% relative to a 7.5 by 7.5 cm NaI(Tl) crystal. During in-beam gamma-counting, the resolution had a value of 2.6 keV (0.2 %) at 1.3 MeV and of 6 keV (0.09 %) at 7 MeV. This good resolution allowed the complex features of the recorded gamma-ray spectra to be well revealed.

The detector signals were processed by conventional amplifiers and 100 MHz ADCs. Because a gamma-energy range from 0.1 to 8 MeV had to be covered, 8000 channels were required for the spectrum conversion. Therefore, the spectrum was divided into two parts by means of a biased amplifier and stored in two 4K multichannel analysers. The low and the high energy part of the spectrum were choosen in such a way that an overlapping range existed. The low-energy part produced a high deadtime of about 15 %, while the high-energy part had a very small one. Count rates and peak areas in the energy range common to both analysers provided additional control of deadtime corrections.

The gamma-ray spectra were unfolded by an interactive computer program using a modified Gauss-Newton algorithm with polynomial continuum of optional degree and FWHM calibration [Kruse, 1979]. Optical inspection of peak fits on a graphical terminal and a reduced chi-square value were used to decide if a special region of the spectrum was fitted satisfactorily. The energy calibration was performed by means of a linear regression with selected peaks. A prompt gamma-ray library containing about 650 full energy lines provided the data base, which permitted the evaluation program to identify the possible source reactions of detected peaks.

In order to check the linearity of the GRS in the high-energy energy range, an iron target was irradiated. The measured energies of Fe neutron-capture lines agreed within a range of ± 1 keV with values by Stelts and Chrien [1978]. In addition, it turned out, that the energy values of different authors were compatible within a limit of ± 2 keV.

Numerical Evaluation

In order to calculate the gamma-ray line flux from the net peak areas, several corrections have to be applied including a systematic error propagation.

Total neutron flux. To be able to compare different target irradiations, the integrated neutron flux has to be determined. Because of the experimental set-up, a direct integration of the flux couldn't be achieved, but an indirect method was applied. The total induced gamma-radiation is a function of the neutron source strength provided the set-up stays the same except for the target material. Most gamma rays are from the background and thus vary directly with source strength. Integrating over the entire gamma-spectrum gives a number that corresponds to the integral source strength neglecting the specific target contribution. Relative flux correction factors normalize the peak areas of each irradiation to a standard flux with an estimated error of about 10 %.

Subtraction of background radiation. As mentioned above, there is a discrete energy gamma-ray background. Therefore, irradiations

without a target were carried out and the accumulated gamma-ray background was determined. For target irradiations, the net target signals result from the difference of total peak area and background component both corrected for neutron flux. The error of this subtraction can be large if the two components have the same order of magnitude, which can happen for certain elements. Therefore, this error shows the quality of the target signals.

Efficiency calibration. Cross sections for photoelectric absorption, Compton scattering, and pair production together with crystal volume, geometric shape and other parameters, determine the efficiency of a Ge detector for incoming gamma rays. The energy dependence of the efficiency is measured by well-known gamma-ray line intensities over the entire energy range up to 8 MeV.

The efficiency measurements were carried out by using the gamma-ray lines of a calibrated Ra-226 source for the low-energy range and the neutron-capture reaction lines of Fe-56 for the high-energy part. The Ra source was counted without detector shielding, the Fe-target with shielding but corrected for gamma absorption (see below). Effects of different lateral size of the sources were neglected. The two data sets were adjusted to each other due to their common energy range and the data points were fitted by a special polynomial (Figure 2). This procedure led to a mean error of about 5 % for the efficiency correction [Brückner, 1984].

Efficiency of escape peaks. Pair-production of high-energy gamma rays leads to single and double escape peaks in the spectra.

The efficiency ratios of single and double escape peaks over their full-energy peaks vary with energy. These reactions reveal the ability of the detector to absorb high-energy gamma rays by multiple interactions processes. For the used Ge crystal having a length of 48 mm and a diameter of 52 mm, single and double escape peaks reach the same efficiency as their full-energy peak, for gamma-ray energies of 6.3 and 6.9 MeV, respectively. Therefore, escape peaks can be a valuable tool for analysis because the information for a single gamma-ray line is given by three peaks.

Gamma-ray attenuation in the shielding. The Ge detector is shielded by boric acid, paraffin, wood, and collimating lead as described above. The gamma rays penetrating the shielding are attenuated due to the total mass attenuation coefficient of the complex shielding and to the energy of the gamma rays. Since no irradiation without shielding could be carried out, the ratio of attenuated to non-attenuated gamma-rays per energy had to be calculated. The attenuation correction factor had an energy-dependent error starting with 13 % for 200 keV and decreasing to 8 % for 8 MeV [Brückner, 1984].

Gamma-ray attenuation in the target. Neutrons induce gamma rays in every depth layer of the target. Therefore, the target material itself attenuates the emerging gamma rays due to its mass attenuation coefficient. To calculate the attenuation a formula for the gamma flux from an infinite plane given by Gorenstein and Gursky [1970] and Reedy et al. [1973] was applied but had to be modified because of the finite size of the target. Using the mass

attenuation coefficients compiled by Hubell [1969], the attenuation correction factor had a mean error of about 3 % [Brückner, 1984].

Results

Gamma-ray Lines

The complete gamma-ray spectrum recorded during the irradiation of an iron target is shown in Figure 3a and 3b. First, the gamma-rays of the surrounding matter as germanium, aluminum, lead, boron, paraffin, concrete, etc. are discussed, then the target ones. Most gamma-ray energies, if not quoted otherwise, can be found in Reedy [1978].

Germanium. The spectrum shows peaks which result from the interaction of neutrons in the germanium crystal. Two narrow lines at 140 and 198 keV are produced by the de-excitation of isomers of Ge-75 and Ge-71, respectively, after neutron capture [Morinaga and Yamazaki, 1976]. The 198 keV peak is a sum peak of 23-keV plus 175-keV. The latter one can also be detected as a weak single line. The Ge gamma-ray line at 868 keV does not show any noticeable broadening.

Between 0.5 and 1.1 MeV, five wide, asymmetric peaks can be observed (Figure 4). These peaks have a steep drop at the lower energy side but a very slow drop (about 50 keV) at the higher one. The energies at the lower edges correspond to levels in various Ge isotopes: 563 keV in Ge-76, 596 keV in Ge-74, 693 and 835 keV in Ge-72, and 1040 keV in Ge-70. The 596-keV peak is also made by a neutron capture reaction, hence the narrow peak on the top. These broad peaks were made by scattering reactions where an energetic

neutron excites a Ge nucleus to a level that rapidly de-excites. This de-excitation energy is often increased in the Ge crystal by the addition of energy from the recoil of the excited nucleus [Bunting and Kraushaar, 1974]. Because the amount of recoil energy varies statistically, a sawtooth-like shape of the peak is produced.

Fortunately, these Ge background features occur in energy regions where one does not expect to have many gamma-ray lines of interest from a planetary surface. The strongest interference probably would be for the 844 and 847 keV scattering lines from Al and Fe, which are located on the slope of the broadened 835 keV peak of Ge.

Aluminum. Due to the conventional construction of a detector, neutrons induce gamma rays in the aluminum end cap. The strongest Al line (1779 keV) results from the beta-decay of Al-28, which is formed by neutron capture. Two gamma-lines, 844 keV and 1014 keV, are produced by $^{27}Al(n,n\gamma)$ and $^{27}Al(n,p)^{27}Mg$ reactions. Under the given energetic conditions, a rather rare (neutron,deuteron) reaction is observed: the 1809 keV line of $^{27}Al(n,d\gamma)$. At 2210 keV, a weak scattering line can be detected that is interfered by the increasing shoulder of the extreme strong hydrogen peak at 2223 keV (an Al spectrum is shown in Brückner et al. [1984]). A weak capture line can also be found at 7724 keV, but its two escape peaks were usually buried by the Compton background of Fe lines. The discrete energy background induced in the aluminum end cap sets severe restrictions to the sensitivity of Al target lines.

Lead. Because lead is the innermost shielding material, all neutron-induced lead gamma rays were investigated by means of an additional lead target and their energies were compared with literature values [Bird et al. 1973, Cranberg et al. 1967, Nellis et al. 1974]. In the energy region from 0.5 to 1.2 MeV, there are several weak scattering gamma-ray lines such as 538 and 881 keV of Pb-206, 898 keV of Pb-207, and 583 keV of Pb-208. Two strong scattering lines can be seen at 803 keV of Pb-206 and at 2615 keV of Pb-208. In addition, two (n,2n) reactions with Pb-208 produce strong peaks at 570 and 1064 keV. In almost all cases, these background Pb-lines do not interfere with target lines of interest.

Boron. The next consecutive shielding material is boron which has a very high thermal cross section for the $^{10}B(n,\alpha)$ reaction producing an excited nucleus of Li-7. The 478 keV de-excitation line of Li-7 shows a Doppler broadening that results from the recoil energy transfer of the emitting Li nucleus to the gamma quantum [Jurney, 1979]. The broadening is symmetric to the net transition energy of Li-7. Additional boron lines could not be detected.

Hydrogen. Hydrogen is one of the major constituents of the outermost paraffin shielding. It has a relatively high cross section of 0.3 barn for neutron capture. Therefore, a very large peak is present at 2223 keV, plus its two escape peaks. The foot of this giant full energy peak is so extended that a Al line at 2210 keV is severely interfered. The big amount of paraffin was necessary only in this experiment; under different operating

conditions, much less paraffin may be required and none is required in space missions.

Carbon. Carbon is the other major constituent of paraffin and its major reaction $^{12}C(n,n\gamma)$ leads to an excited level at 4438 keV. Because of the short half-life of 43 fs and of the excited nucleus' recoil, the deexcitation gamma-ray line is broadened by the Doppler effect. So we find a big bump in the energy region around 4440 keV plus two escape bumps.

To investigate the shape of the carbon bump (Figure 5) a thick paraffin target was irradiated in order to have a larger mass at the target place compared to the paraffin shielding. The position of the single escape peak of the $^{28}Si(n,\gamma)$ reaction sitting on the bump indicates very easily that there is a 15-keV shift of the maximum of the bump compared to the energy of the first C-12 level. The shift results from the geometrical arrangement of neutron source, target, and detector: 14-MeV neutrons moving towards the detector transfer kinetic energy to the carbon nuclei of the target. According to the Doppler effect, gamma rays reaching the detector show an increase in frequency that is overlayed by the random motion of the recoiling carbon nucleus. This motion leads to a FWHM of 53 keV, which is more than a factor of 10 larger than a non-broadened peak like the 4.8-keV FWHM of the nearby Si peak.

Comparing the shape of the carbon bump in our spectra with investigations of Janout et al. [1980], it is seen that the experimental configuration is responsible for the specific shape of a Doppler broadened peak. This broadening of the 4438-keV gamma ray reduces the sensitivity for carbon tremendously. Because of the

very small cross section of the neutron-capture reaction only a weak capture line from carbon can be observed at 4946 keV, which can be interfered by a weak Fe line.

Oxygen, silicon, and calcium. The concrete shielding wall produces background gamma-ray lines for oxygen, silicon, and calcium.

A very strong neutron scattering line at 6129 keV and its two escape peaks result from O-16. Two $(n,\alpha\gamma)$ reactions of O-16 can be observed at 3854 and 3684 keV, plus their escape peaks.

Si gamma rays can be found all over the spectrum. Strong Si lines are produced by neutron-capture reactions at 4934 and 3539 keV including their escape peaks, weak ones at 2093 and 6381 keV. The first level of Si-28 is a strong interference for the 1779-keV line of Al-28. Weak scattering lines can be detected at 4497 and 6878 keV.

Ca-40 produces weak peaks only, such as capture reaction lines at 1943 and at 6420 keV and a scattering line at 3737 keV.

Iron. The iron gamma-ray lines result from the iron-target and from the surrounding iron. Most lines are produced by neutron capture and only a few by neutron scattering. The most striking features in the high energy region are three doublets: the full energy peaks at 7631 and 7645 keV and their two escape peaks. The difference between the energies of these double peaks is 14 keV, which demonstrates the good resolution of the Ge detector even in such a high energy region. Other prominent capture peaks of Fe-56, including their escape satellites, can be seen at 4218, 5920, 6018,

and 7279 keV. In the low-energy range large peaks are found at 692, 1613 and 1725 keV, where the first is superimposed on a Ge sawtooth peak. Many weak Fe peaks can be observed in addition but are not listed here.

Neutron scattering produces two dominant lines at 847 and 1238 keV corresponding to the energies of the first two levels of the Fe-56 nucleus. Two weak scattering lines of Fe-56 can be observed at 1038 and 2113 keV, where the former is interfered by a Ge sawtooth peak. One scattering reaction results from the second most abundant Fe isotope, the Fe-54 nucleus, identified by the 1408-keV line. Two (n,2nγ) reaction lines are represented at 931 and 1316 keV. Expected but weaker scattering lines at 2523, 2601, and 3602 keV could not be detected under the given experimental conditions.

Neutrons

In order to interpret the recorded gamma-ray spectra in greater detail, it is necessary to know the energy distribution of the neutrons reaching the target. The 14-MeV neutron generator used in this experiment produced a maximum source strength of $2 \cdot 10^{11}$ neutrons/s. The flux at target position had a maximal value of 10^4 neutrons/$cm^2 \cdot s$, which was measured by foil activation technique selecting reactions with suitable cross section, half-life, and threshold energy, c.f. Table 1. Activated foils were counted by a large (200 cm^3) Ge(Li) detector calibrated for absolute efficiency.

Cadmium ratio. The thermal and epithermal flux was determined by irradiating a bare Au foil together with a Au foil that was covered by a thermal neutron filter. Either cadmium or boron serve

the purpose [Ehmann et al., 1980], but for simplicity a neutron-tight Cd container was used. Neutron selfabsorption had to taken into account for the Au foils. Factors determined by Albert [1962] were applied for correction to a thickness of zero, while due to criteria of Beckurts and Wirts [1964] no corrections were necessary for the other foils. The cadmium-ratio that is the ratio of the activity induced by the total flux to the one induced by the epithermal flux [Steinnes, 1971] had to be modified applying considerations of Albert [1962]. At target position, we measured a cadmium-ratio of 2.0 ± 0.1 [Brückner, 1984]. This means that the thermal to epithermal component is rather low compared to a well moderated spectrum. A similar value (2.1) was observed in the lunar surface at a depth of 180 g/cm^2 [Burnett and Woolum, 1974]. In spite of the different production and moderation conditions in the lunar surface and in our experiment, this similarity has to be noted and will allow us to test assumptions used to calculate lunar neutron-capture gamma-ray fluxes.

Neutron spectrum. The fast flux was detected by two Al reactions, which have different threshold energies. For the (n,p) and (n,α)-reaction in the 8 to 14 MeV region, the cross section of 14 MeV was used as a mean value: 78 mb and 120 mb, respectively [Bayhurst et al., 1975, Bormann et al., 1974, Husain et al., 1970, Salaita, 1971, and Vonach et al., 1970]. For the (n,p)-reaction in the region of 6 to 8 MeV, a cross section of 67 mb was adopted.

Combining the results of Au, Al, and Cu reactions, the differential neutron spectrum is obtained and shown in Figure 6. The dotted line serves to guide the eyes, but it also may suggest

intermediate values. At 14 MeV, there is a small peak in the spectrum that results from the experimental set-up. A certain amount of 14-MeV neutrons can travel to the target without interactions, while for neutrons emitted not towards the target, the probability of reaching the target increases with an increasing number of scattering processes. Hence, energies just below 14 MeV are more unlikely get position than lower ones. In spite the fact that only fi .ctions for unfolding the neutron spectrum could be used, some typical features can be recognized.

Thermal and 14-MeV flux. During in-beam gamma-counting the neutron flux at target position was so weak that only the BF_3-monitor (Figure 1) could be used counting neutrons. Therefore, the BF_3-monitor was calibrated to the source strength of the 14-MeV neutron generator by irradiating Cu foils for different neutron fluxes. The ratio of 14-MeV to thermal neutrons at target position was measured by simultaneous irradiation of Cu and Au foils. Combining BF_3-monitor and foil data typical values for thermal flux and 14-MeV at target position (during in-beam counting) were determined to 440 and 100 neutrons/$cm^2 \cdot s$, respectively [Brückner, 1984].

Gamma-ray Flux

Targets consisting of one or several major elements were selected for prompt gamma-ray production. Table 2 gives data on the target material including the macroscopic cross section that is defined as the product of cross section σ and number of nuclei per cm^3. The targets had a mean area of about 0.6 m^2, their depth

varied depending on fabrication conditions. As long as the targets are sufficiently thin, the spectral shape of the neutron flux is not affected, i.e. each target is exposed to the same neutron spectrum. In addition, the gamma-ray emmision is corrected for self attenuation in the target.

The concrete target was not a thin target in the sense of neutron interaction, but it was used for the study of relative thermal line fluxes. As a result of depth, density, and cross section the macroscopic cross section of the targets varies several orders of magnitudes, as indicated for capture reactions in Table 2. Because of these and other parameters, the gamma-ray flux of different elements has a large variation using the same neutron flux. The irradiation of monoelement targets facilitates the study of prompt gamma-ray production, but it does not eliminate the disadvantage of a wide sensitivity range.

In order to achieve sufficient counting statistics for high energy peaks, 11 hours of counting were necessary. With the given electronics a mean count rate of about 6000 counts/s was obtained without spectral distortions.

Iron target. The Fe target has a purity of 99.9 % and weighs about 50 kg. For thermal reactions it has the highest macroscopic cross section of 0.22 cm^{-1} (Table 2). The spectrum is seen in Figure 3 and comments were given above. For the calculation of the line fluxes all the mentioned corrections were applied to the peak area. In order to show the influence of this correction procedure, selected lines are listed in Table 3 together with their peak area including their statistical error and their flux with an error

resulting from error propagation.

It turns out that the flux of most of Fe (n,γ) lines in the high energy region has an error between 15 and 20 %, which is relatively small for this type of experiment. The correction for total neutron flux already contributes an error of 10 % and the subtraction of the discrete background can produce a rather large error due to subtraction error propagation.

The influence of background subtraction can be seen for scattering reaction peaks in the low energy region: the strong 847 and 1238 keV peaks with very small errors of about 1 % have a large flux error of 39 and 46 %, respectively. For the weak peak at 1811 keV with a small error of 5.5 %, no target signal that was statistically meaningful could be extracted. The two lines at 931 and 2113 keV have a flux error that lies above the limit for a relevant statistical signal. Three expected scattering lines at 2523, 2601,and 3602 keV could not be detected, their detection limit is determined calculating a fictitious peak area with 50 % standard deviation.

Gamma-ray flux of Fe. The neutron-capture induced gamma-ray flux of Fe can be used to check the overall correction, because the yield of the lines is controled by the deexcitation process of the nucleus. The measured flux of eight neutron-capture lines of Fe were compared with literature values [Stelts and Chrien, 1978]. As Figure 7 shows, the Fe flux ratios deviate within 10 % of the relative thermal yields. These Fe gamma-ray fluxes demonstrate that the corrections, especially for attenuation, were well made for

this type of experiment. The good agreement for neutron-capture gamma rays between the measured fluxes and the thermal yields show that the effects of epithermal reactions can be neglected and that the yields for the capture of thermal neutrons can be used for the complex spectrum of low-energy neutrons present in a planetary surface.

The results of the Fe target experiment point out the intrinsic characteristics of prompt gamma-ray spectroscopy in an environment with high discrete and high continuous background (a situation that probably could be encountered during a planetary mission but not as seriously as here). To complete the study results of additional targets are briefly presented.

Aluminum target. The Al target consists of an Al-Mg-Si alloy with Mg and Si in a low concentration of about 1 %. Al has a macroscopic cross section of 0.014 cm^{-1} (Table 2), which compared with Fe will produce a much weaker target signal. In addition, the detector end cup is made out of Al, as already mentioned, which provides a prominent interfering source.

These two facts deteriorate the statistical separation of the target signal from the discrete line background, as indicated in Table 4. Only the high-energy triplet of the 7724-keV line produces a significant target signal. Large errors of the target signal are found for the low-energy lines at 844 and 1014 keV. Even the strongest Al peak (1779 keV) shows no statistically meaningful contribution from the target. A similar fate holds for the 1809 keV line. Two expected scattering lines at 2981 and 3004 keV could not be detected.

The reason why the high-energy target signals can be better determined depends on several facts, such as error propagation, different distance of target and end cup to the crystal, and energy dependent gamma-ray attenuation.

These results demonstrate the difficulties of using an Al end cup and measuring Al gamma-ray lines. This problem will also arise during a planetary mission if the detector is surrounded by a lot of Al, which may be inevitable due to construction constraints.

Silicon target. The silicon dioxide target, which simply is called a Si target, consists of pure SiO_2, which is made by sintering quartz powder and can be purchased in plates. Si has a low thermal macroscopic cross section of 0.0014 cm^{-1}. But due to the high abundance of Si and O in rocks compared to other major elements, the Si and the O lines will be very prominent.

This is verified in the Si spectrum, where most of the expected strong Si peaks have an error below 10 % (Table 5). But the corresponding flux errors are above 50 %, which seems to be surprising. Keeping the experimental set-up in mind, it has to be noted that almost all the surrounding material consists out of concrete, i.e. tons of Si and O. The large flux errors are merely the result of a low mass ratio of target to surrounding matter. To improve this, a thick concrete target was additionally irradiated.

Si peaks were selected for Table 5 only if they had more than 1000 counts. The two strongest neutron-capture peaks at 3539 and 4934 keV have counting errors below 2 % but flux errors above 50 %. The very strong 1779 keV line is produced by several reactions, as the scattering line $^{28}Si(n,n\gamma)$, the two beta decaying lines $^{28}Si(n,p)^{28}Al$ and $^{27}Al(n,\gamma)^{28}Al$ (resulting from the end cup).

Some expected scattering lines could be detected at 2235, 2839, 4497, and 6878 keV (plus escape peaks). The 2235 keV line is heavily interfered by the very strong H peak at 2223 keV, which will usualy not happen during planetary counting.

Magnesium target. An alloy of 90 % Mg, 9 % Al, and 1 % Zn was used as target material. The thermal macroscopic cross section of Mg is 0.0025 cm^{-1}, which has the same order of magnitude as Si. Therefore, similar restrictions in the target flux evaluation are encountered as mentioned above. A list of Mg gamma-ray lines is given in Table 6. The lowest energy gamma-ray line at 1130 keV results from a scattering reaction with Mg-26. The largest Mg peak at 1368 keV is produced by two reactions: $^{24}Mg(n,n\gamma)$ and $^{24}Mg(n,p)^{24}Na$. The decay of 15-hour Na-24 produces two gamma rays in cascade (2754 and 1368 keV). The flux ratio of the two lines shows that the scattering reaction provides a strong contribution to the 1368 keV line. Na-24 can also be produced by an $Al(n,\alpha)$ reaction and at higher energies by Si spallation. The Mg 1809-keV gamma-ray is also a product of two reactions, neutron scattering and capture. Interferences can result from Fe gamma rays and from the decay of the long-lived radionuclide Al-26, not relevant for this experiment.

The capture reaction lines at 2829 and 3918 keV form a double peak with O and Si lines, respectively, which can be deconvoluted by the evaluation code. Two expected scattering reaction lines at 3867 and 4238 keV could not be detected.

Concrete target. The thickness of the concrete target having a value of 30 g/cm^2 exceeds the thickness of the other targets by far. Therefore, it cannot be considered as a thin target, i.e. the assumption that the neutron flux is not altered by the target is not valid anymore. The purpose of the thick target irradiation was to increase the flux of some target reaction lines, to study thermal neutron-induced reactions of different elements beeing exposed to the same neutron flux, and to examine some scattering reaction lines.

To determine the composition, 4 kg of the target were ground and homogenized, and 100 mg were prepared for the analysis. Ca and Fe were determined by instrumental thermal neutron activation analysis [Wänke et al., 1977], O, Mg, Al, and Si by instrumental fast (14-MeV) neutron activation analysis [Hofmeister, 1977]. The composition is found in Table 7. The concentration of H and C were estimated according to the typical composition of concrete having a density between 2.2 and 2.4 g/cm^3 [Lindackers, 1962]. Results of the target irradiation are given in Table 8.

H doesn't show a significant contribution from the target due to the high H concentration in the paraffin shielding. Fe capture reactions lines from the target could not be identified. The reason is the very low Fe content of the target. Similar results are found for Mg reaction lines. The Al peaks produced by the target are very weak and are only detectable in the high-energy region. The largest peaks result from the $^{16}O(n,n\gamma)$ reaction where the contribution of the $^{16}O(n,p)^{16}N$ reaction is very small due to its relatively low cross section. Several Si lines could be found. The strongest peak results from the 4934-keV gamma-ray line that is also used for the normalization of all other fluxes in Table 8.

Concrete was the only target where Ca gamma rays could be studied. There are two rather strong capture reaction lines at 6420 and 1943 keV. Also, one of two expected neutron scattering reaction lines of Ca-40 could be observed. The 3737-keV line was significantly above the background. The other line at 3904 keV could not be detected. The predicted flux of the unobserved 3904-keV gamma-ray line from Ca-40 was about 0.6 of that for the 3737-keV line [Reedy, 1978]. The mean lifes of the 3737- and 3904-keV levels of Ca-40 are 68 and 0.05 ps, respectively. The fact that the 3904-keV gamma ray was not observed could be the result of Doppler broadening produced by the recoil energy of the excited Ca-40 nucleus.

Flux ratio. The gamma-ray lines produced by the concrete target allow us to compare measured flux produced by Al, Ca, and Si with calculated fluxes according to the composition of the target (see Table 9). The calculated and measured fluxes agree within an error limit of 20 %, a good result for an experiment of this type. The only large deviation is found for the 1943-keV line from Ca. Here, we have a discrepancy of almost 40 % [Reedy, 1978] that should be investigated in future experiments.

Discussion

The effective neutron source used in this work has a two-component structure: the point-like 14-MeV neutron generator and the spatial extension of the neutron backscattering walls. At target position, the 14-MeV and the thermal flux was about 100 and 440 neutrons/$cm^2 \cdot s$, respectively. The total neutron flux on the

moon, for example, is about 12 neutrons/cm•s [Burnett abd Woolum, 1974]. The corresponding component below 3 eV was estimated to be 3.6 neutrons/cm^2•s [Lingenfelter et al., 1972].

To estimate the ratio of gamma to slow neutron flux, the 7.6-MeV capture reaction line of Fe can be used. The gamma-ray flux of this line in our experiment was 15 photons/cm^2s. In a 100 km lunar orbit a flux of 0.0092 photons/cm^2s is expected for the same line [Reedy, 1978]. Due to self attenuation of gamma rays in the lunar surface, an effective area of about 100x100 km can be assumed [Reedy et al., 1973] compared to a target area of 70x100 cm at a distance of 20 cm in this experiment. The ratio of gamma to neutron flux of the 7.6-MeV line for this work and the Moon is 0.034 and 0.0025, respectively. This is a result of difference in solid angle of target area to detector, thickness of target material (self attenuation), and neutron production mechanism. This points out that a thin target experiment has to be considered as a qualitative simulation of planetary gamma-ray production.

The gamma-ray spectra obtained in our experimental configuration show gamma-ray lines of all major elements. The complexity of the spectra can be considered to resemble spectra recorded in a planetary orbit. Of course, lines emitted by long-lived radionuclides and spallation reactions are missing. Depending on the hydrogen (water) content of the planetary surface, the ratio of capture reactions to scattering reactions will vary. In this work, a hydrogenous environment, like the Martian polar caps or a comet nucleus, was simulated.

Besides the discrete gamma-ray lines of interest, lines were produced by the surrounding material. In addition, the major part

of the gamma radiation emitted by the target and the surrounding material belongs to the gamma continuum. Therefore, the spectra show a rather high background with overlaying peaks. All these features will be encounterd in planetary spectra, too. Cosmic rays induce gamma radiation in the surface, the spacecraft, and the detector assembly.

To resolve all the spectral features, an energy conversion of 1 keV per channel was used, i.e. 8000 channels for an energy interval from 0.1 to 8 MeV. The upper limit of about 8 MeV excludes a few possible gamma-ray lines, but most of the elements under question have stronger lines below 8 MeV, except for Ni. If one uses spectra compression, a higher upper threshold can be achieved, a trade-off to a linear relationship between energy and channel number.

Detecting Neutrons

An orbiting planetray GRS receives besides gamma rays also neutrons either emitted by the surrounding material or by the planetary surface, the albedo neutrons. Because the neutron flux is a function of the cosmic-ray flux, variations in the cosmic-ray flux can be monitored by measuring these neutrons. In this way, spectra recorded periodically over the same surface area can be normalized to the same cosmic-ray flux. Care has to be taken that there is no change in the hydrogen content in the subsurface layers.

One method of detecting neutrons is to measure gamma rays that are indicative of neutron-induced reactions. The different Ge isotopes of the detector crystal are a source for such

neutron-induced gamma rays that produce narrow and sawtooth-shaped peaks in the spectra. The shape of the broadened peaks depend on the energy of the incident neutrons [Chasman et al., 1965]. Therefore, investigations using neutrons with different energies should be carried out.

Placing boron close to the detector, the 478-keV gamma-ray line of B-10 is a monitor for thermal and epithermal neutrons. These and other methods as the use a thin neutron absorber surrounding the gamma-ray detector, can be applied for monitoring albedo neutrons [Haines and Metzger, 1984b].

Signals from Different Sources

The study of different targets demonstrated the feasibility of prompt gamma-ray spectroscopy under the given experimental conditions, i.e. the amount of radiation emitted by the target and by the surrounding material. During a planetary mission the same questions concerning the different sources of radiation arises and can be anticipated as a short overview will show.

The material that is closest to the detector is the Al of the detector end cap. The experiment showed that the high-energy lines were best suited for the determination of the target Al. Care has to be taken that there is not too much Al close to the detector in order to be able to extract the target signal from the total Al signal. On a spacecraft, most of the construction material will be Al. The contribution of the spacecraft to the Al background can be reduced by mounting the Ge detector assembly on top of an extensible boom that will also reduce the background from other elements on board of a spacecraft.

To reduce further the Al background, different end cap material could be used, e.g. Cu. An electrolytic Cu end cap is commonly used for low-level counting because it does not contain Th as even high-pure Al does (a Th-free end cap is also very suitable for the measurement of Th in a planetary surface). But Cu produces many gamma rays over the entire energy range and some lines interfere with lines of interest. Using Mg as material for the end cap, will create similar restrictions for the Mg measurements of the surface as mentioned for Al. In the view of the requirements the choice of the best end cap material is a trade-off.

In our experiment, Si and O were the major constituents of surrounding material and produced a large Si and O background. On a spacecraft, there will be not very much Si except for electronic chips and solar paddles. The use of a boom will reduce their contribution and the planetary surface will be the major source for Si gamma rays

The Fe lines in our experiment showed only a rather small background contribution that permitted a good extraction of the target Fe signal. Some parts of a spacecraft may be fabricated out of steel, but here the boom will be helpful, too. If the Fe content in the surface is not too low, the ratio of thermal and fast neutron-induced reaction lines could be used to look for variations of the neutron flux in subsurface layers, as the ratio of neutron-capture to nonelastic-scatter gamma rays increases with higher hydrogen contents [Lapides, 1981].

Because Ca is normally not present on a spacecraft, the surface will be the only source and therefore, Ca will be measured without interferences.

Oxygen produced very prominent neutron-induced scattering reaction lines in the experiments. In a planetary surface it will be easily detected, too. For most of the expected surface rocks, their O content is not expected to vary much. Therefore, deviations from the mean O gamma-ray flux will give a fast hint to special features such as ore deposits, ice layers, etc..

In our experiment, most of the H could be found in the paraffin shielding, but also some in the concrete walls. The concentration of H and H_2O in a surface is of importance for the neutron moderation and for the interpretation of compositional data concerning planetology, cosmochemistry, etc. [Dreibus and Wänke, 1985]. Some background will be produced by parts of the spacecraft, the plastic scintillator that will surround the detector in order to cancel out signals from charged particles, and fuel for propulsion. The amount of fuel will decrease during the mission, but this can be measured and corrected for.

The analysis of C is limited by the Doppler broadening of the most intense gamma-ray line, which reduces the detection limit of C very much. Interferences will originate from almost the same spacecraft components as mentioned for H. If the the C content of a planetary surface is high enough, the broadened C line may be measured, or if the thermal neutron flux is high enough, the narrow weak neutron-capture line may be detected. In cometary nuclei the C analysis may be carried out provided the composition corresponds to conventional models, as dirty snowball [Delsemme, 1982].

The importance of measuring natural radionuclides, such as K, Th, and U in planetary surfaces [Wänke, 1981] leads to the requirement of constructing a spacecraft that is radioactively clean, especially parts close to the detector.

Line Width

The gamma-ray spectra of these experiments show that most of the gamma-ray lines do not show a severe broadening, except for Ge, C, and B peaks. In planetary surfaces, neutrons can have energies up to 100 MeV, while the majority will be below 10 MeV [Reedy and Arnold, 1972]. Therefore, the search for Doppler broadening by using neutrons with energies above 14 MeV should be carried out, especially, because theoretical predictions on the detection limit of elements depend on the line width.

Radiation Damage

The time of flight of a spacecraft to a planetary body and the data taking phase will be of the order of years. The continuous bombardment of cosmic-ray particles while in space causes a build-up of radiation damage that will change the properties of a HPGe detector, i.e. the resolution can degrade so badly that the detector is not useful for measurements anymore. To overcome detector failure one can remove radiation damage by annealing the Ge crystal at elevated temperatures [Pehl et al., 1978] or one tries to avoid annealing by using a detector type that has a good radiation damage resistance. For neutron bombardments the n-type HPGe detector shows a better resistance than the p-type detector [Pehl et al., 1979]. But it remains open, which type of HPGe detector is more suitable for a long space mission concerning radiation damage induced by low-flux GCR and by high-flux SCR particles and mechanical sturdiness for possible annealing procedures.

Two times during our experiments, the accumulated radiation damage of the Ge crystal had to be annealed. These repairs were not

unexpected [Kraner et al., 1975, Kraner, 1980], because the experimental set-up caused the absorption of a rather high neutron dose.

Conclusion

This experiment investigated prompt gamma rays induced by neutrons with a maximum energy of 14 MeV. The agreement of measured flux ratios of neutron-capture lines with theoretical values showed that thermal cross sections can be applied to the low-energy neutron spectrum produced in a planetary surface, i.e. gamma-ray fluxes, detection limits, and element concentrations can be calculated using these cross sections. For radioactive elements the concentration calculation is rather straight forward because it depends only on well-known physical parameters. But for elements measured by their cosmic-ray induced gamma-radiation, their concentration variations can only be mapped by using a detailed model describing flux and spectrum of secondary particles as a function of depth, cross section, and composition. Such a model can be checked and improved by using accelerator bombardments of targets with known composition and possible 'ground truth' of known planetary sites. In case of lack of ground truth values, a refined model is required that uses the preliminary concentration data in order to vary the model concentrations in such a way that the measured gamma-ray flux is reproduced. If one can detect all major elements, the sum of the abundances can be normalized to unity.

The present study was a first step towards a more realistic simulation of of the total process of cosmic-ray interactions with a surface and of gamma-ray spectra recorded by a Ge detector

operating in the orbital radiation environment of a planetary body. Further experiments are required to investigate more aspects, such as a study of nonelastic scatter reactions induced by high-energy neutrons, an experiment that was recently carried out at the cyclotron of the KFA Jülich, F. R. Germany, [Brückner et al., 1985]; a study of radiation damage build-up in Ge detectors bombarded by high-energy, low-flux protons and implications for gamma-ray spectra recorded under planetary radiation conditions, an experiment we will carry out at the accelerator of SIN, Switzerland; a study of interactions of high-energy protons with matter and of resulting gamma-ray radiation, an experiment we intent to do at an accelerator providing us with GeV protons; and a study to adapt present-day gamma-ray spectra evaluation techniques to the specific needs of planetary gamma-ray spectroscopy.

Acknowledgement

We would like to thank H. Kruse for software assistance, and K. Blum and H. Hofmeister for discussions and help for the experimental set-up.

References

Albert, D., Korrektionsfaktoren für dicke Goldsonden, Kernenergie 5, 154-157, 1962.

Arnold, J.R., A.E. Metzger, and R.C. Reedy, Computer-generated maps of lunar composition from gamma-ray data, Proc. Lunar Sci. Conf. 8th, 945-948, 1977.

Bard, S., J. Stein, and S.W. Petrick, Advanced radiative cooler with angled shields, Prog. Astronautics Aeronautics 83, 249-258, 1982

Basaltic Volcanism Study Project, Basaltic volcanism on the terrestrial planets, Pergamon Press, Inc., New York, 1981.

Bayhurst, B.P., J.S. Gilmore, R.J. Prestwood, J.B. Wilhelmy, N. Jarmie, H. Erkkila, and R.A. Hardekopf, Gross sections for (n,xn) reactions between 7.5 and 28 MeV, Phys. Rev. C 12, 451-467, 1975.

Becker, R.H. and R.O. Pepin, The case for a martian origin of the shergottites: nitrogen and noble gases in EETA 79001, Earth Planet. Sci. Let. 69, 225-242, 1984.

Beckurts, K.H. and K. Wirtz, Neutron Physics, Springer-Verlag, 1964.

Bielefeld, M.J., R.C. Reedy, A.E. Metzger, J.I. Trombka, and J.R. Arnold, Surface chemistry of selected lunar regions, Proc. Lunar Sci. Conf. 7th, 2661-2676, 1976.

Bird, J.R., B.J. Allen, I. Bergqvist, and J.A. Biggersraff, Compilation of keV-neutron-capture gamma-ray spectra, Nuclear Data Tables 11, 433-529, 1973.

Bormann, M., H. Neuert, and W. Scobel, Tables and graphs of cross-sections for (n,p), (n,α) and (n,2n) reactions in the neutron energy region 1-37 MeV, in Handbook on Nuclear Activation Cross-Sections, IAEA, Vienna, 1974.

Brückner, J., Neutronen-induzierte Gamma-Spektroskopie: Beitrag zur chemischen Fernerkundung von planetaren Oberflächen, Ph.D. Thesis, University of Mainz, F. R. Germany, 1984

Brückner, J., R.C. Reedy, and H. Wänke, Neutron-induced gamma rays from thin targets: Simulations for planetary sepctroscopy, Lunar and Planetary Science XV, Lunar and Planetary Institute, Houston, pp. 98-99, 1984.

Brückner, J., P. Englert, R.C. Reedy, and H. Wänke, Simulation experiments for gamma-ray mapping of planetary surfaces: scattering of high-energy neutrons, Workshop on Cosmogenic Nuclides, eds. R.C. Reedy and P. Englert, Los Alamos, NM, USA, Lunar and Planetary Institute, Houston, USA, 1985 (in press).

Bunting, R.L. and J.J. Kraushaar, Short-lived radioactivity induced in Ge(Li) gamma-ray detectors by neutrons, Nucl. Instr. Meth. 118, 565-572, 1974.

Burnett, D.S., and D.S. Woolum, Lunar neutron capture as a tracer for regolith dynamics., Proc. Lunar Sci. Conf. 5th, 2061-2074, 1974.

Chasman, C., K. W. Jones, and R.A. Ristinen, Fast neutron bombardment of a Lithium-drifted Germanium gamma-ray detector, Nucl. Instr. Meth. 37, 1-8, 1965.

Cranberg, L., Th. A. Oliphant, J. Levin, and C.D. Zafiratos, Fast-neutron scattering from nuclides in the lead region, Phys. Rev. 159, 969-979, 1967.

Davis, P.A., Iron and Titanium distribution on the Moon from orbital gamma ray spectrometry with implications for crustal evolutionary models, J. Geophys. Res. 85, 3209-3224, 1980.

Delsemme, A.H., Chemical composition of cometary nuclei, in Comets, ed. L.L. Wilkening, The University of Arizona Press, Tucson, AZ, pp. 85-130, 1982.

Dreibus, G. and H. Wänke, The bulk composition of the eucrite patent asteroid and its bearing on planetary evolution, Z. Naturforsch. 35a, 204-216, 1980.

Dreibus, G. and H. Wänke, Mars, a volatile-rich planet, Meteoritics, 20, 367-381, 1985.

Ehmann, W.D., J. Brückner, and D.M. McKown, Epithermal neutron activation analysis using a boron carbide irradiation filter, J. Radioanal. Chem. 57, 491-502, 1980.

Gorenstein, P. and H. Gursky, Characteristic γ- and x-radiation in the planetary system, Space Sci. Rev. 10, 770-829, 1970.

Haines, E.L. and A.E. Metzger, Measuring planetary neutron albedo fluxes by remote gamma-ray sensing, Nucl. Inst. Meth. Phys. Res. 226, 517-523, 1984a.

Haines, E.L. and A.E. Metzger, Measuring planetary hydrogen by remote gamma-ray sensing, Nucl. Inst. Meth. Phys. Res. 226, 509-516, 1984b.

Harrington, T.M., J.H. Marshall, J.R. Arnold, L.E. Peterson, J.I. Trombka, and A.E. Metzger, The Apollo gamma-ray spectrometer, Nucl. Instr. Meth. 118, 401-411, 1974.

Hofmeister, H., Einrichtung eines Meßplatzes zur Instrumentellen Neutronenaktivierungsanalyse (14 MeV) der Hauptelemente in Gesteinsproben, Thesis, University of Mainz, F. R. Germany, 1977.

Hubbell, J.H., Photon cross sections, attenuation coefficients, and energy absorption coefficients from 10 keV to 100 GeV, NSRDS-NBS 29, Nat. Stand. Ref. Data Ser., Nat. Bur. Stand. (U.S.), 1969.

Husain, L., A. Bari, and P.K. Kuroda, Neutron activation cross section at 14.8 MeV for Rubidium, Strontium, Zirconium, and Niobium, Phys. Rev C 1, 1233-1236, 1970.

Janout, Z., S. Pospisil, and M. Vobecky, Observation of a doppler broadening of the 4438 keV gamma-line of ^{12}C in processes $^{12}C(n,n'\gamma)^{12}C$ and $^{9}Be(\alpha,n\gamma)^{12}C$, J. Radioanal. Chem. 56, 71-81, 1980.

Jurney, E.T., Application of the thermal (n,γ) reaction to elemental analysis, in Neutron Capture Gamma-Ray Spectroscopy, ed. R.E. Chrien and W.R. Kane, Plenum Press New York, p. 46, 1979.

Kornblum, J.J., E. L. Fireman, M. Levine, and A. Aronson, Neutrons in the moon, Proc. Lunar Sci. Conf. 4th, Vol. 2, 2171-2182, 1973.

Kraner, H.W., R.P. Pehl, and E.E. Haller, Fast neutron radiation damage of high-purity germanium detectors, IEEE Trans. Nucl. Sci. NS-22, 149-159, 1975.

Kraner, H.W., Fast neutron damage in germanium detectors, IEEE Trans. Nucl. Sci. NS-27, 218-234, 1980.

Kruse, H., Spectra processing with computer-graphics, in Computers in Activation Analysis and Gamma-Ray Spectroscpoy, ed. B.S. Carpenter, M.D.D'Agostino and H.P. Yule, Proc. Amer. Nucl. Soc. Topical Conf., Mayaguez, Puerto Rico pp. 76-84, 1979.

Lapides, J.R., Planetary gamma-ray spectroscopy: The effects of hydrogen and the macroscopic thermal-neutron absorption cross section on the gamma-ray spectrum, Thesis, University of Maryland, U.S., 1981.

Lindackers, K.H., Praktische Durchführung von Abschirmungsberechnungen, Verlag Karl Thiemig KG, München, 1962.

Lingenfelter, R.E., E.H. Canfield, and W.N. Hess, The lunar neutron flux, J. Geophys. Res. 66, 2665-2671, 1961.

Lingenfelter, R.E., E.H. Canfield, and V.E. Hampel, The lunar neutron flux revisited, Earth Planet. Sci. Lett. 16, 355-369, 1972.

Metzger, A.E., R.H. Parker, J.R. Arnold, R.C. Reedy, and J.I. Trombka, Preliminary design and performance of an advanced gamma-ray spectrometer for future orbiter missions, Proc. Lunar Sci. Conf. 6th, 2769-2784, 1975.

Metzger, A.E., E.L. Haines, R.E. Parker, and R.G. Radocinski, Thorium concentrations in the lunar surface. I: Regional values and crustal content, Proc. Lunar Sci. Conf. 8th, 949-999, 1977.

Morinaga, H. and T. Yamazaki, In-Beam Gamma-Ray Spectroscopy, North-Holland Publishing Comp., Amsterdam, 1976.

Nellis, D.O., I.L. Morgan, and E.L. Hudspeth, Neutron-induced gamma-ray production in ^{208}Pb, Phys. Rev. C 9, 1972-1977, 1974.

Ostertag, R., D. Stöffler, H. Palme, B. Spettel, G. Weckwerth, and H. Wänke, Lunar meteorite Yamato 791197: a weakly shocked regolith breccia from the far side of the Moon, Lunar and Planetary Science XVI, Lunar and Planetary Institute, Houston, pp. 635-636, 1985.

Palme, H., B. Spettel, G. Weckwerth, and H. Wänke, Antarctic meteorite ALHA 81005, a piece from the ancient lunar crust, Geophys. Res. Lett. 10, 817-820, 1983.

Pehl, R.H., L.S. Varnell, and A.E. Metzger, High-energy proton radiation damage of high-purity germanium detectors, IEEE Trans. Nucl. Sci. NS-25, 409-417, 1978.

Pehl, R.H., N.W. Madden, J.H. Elliot, Th.W. Raudorf, R.C. Trammel, and L.S. Darken, Jr., Radation damage resistance of reverse electrode Ge coaxial detectors, IEEE Trans. Nucl. Sci. NS-26, 321-323, 1979.

Planetary Exploration Through Year 2000, A core program. Part I. Report by the Solar System Exploration Committee, NASA, U.S. Government Printing Office, Washington, D.C., 1983.

Reedy, R.C. and J.R. Arnold, Interaction of solar and galactic cosmic-ray particles with the moon, J. Geophys. Res. 77, 537-555, 1972.

Reedy, R.C., J.R. Arnold, and J.I. Trombka, Expected gamma-ray emission spectra from the lunar surface as a function of chemical composition, J. Geophys. 78, 5847-5866, 1973.

Reedy, R.C., Planetary gamma-ray spectroscopy, Proc. Lunar Planet. Sci. Conf. 9th, 2961-2984, 1978.

Reedy, R.C., J.R. Arnold, and D. Lal, Cosmic-ray record in solar system matter, Ann. Rev. Nucl. Part. Sci. 33, 505-537, 1983.

Salaita, G.N., Absolute neutron cross sections for the production of the ^{24}Na isomer from Magnesium and Aluminum, Nucl. Phys. A 170, 193-198, 1971.

Steinnes, E., Epithermal neutron activation analysis of geological material, in Activation Analysis in Geochemistry and Cosmochemistry, Universitetsforlaget, Oslo, pp. 113-128, 1971.

Stelts, M.L. and R.E. Chrien, Energies and intensities of thermal neutron capture γ-rays from Cl, Al and Fe relative to N, Nucl. Instr. Meth. 155, 253-260, 1978.

Vonach, H., M. Hille, G. Stengl, W. Breunlich, and E. Werner, Präzisionsmessung des ^{27}Al(n,α)-Wirkungsquerschnitts für 14,43 MeV-Neutronen, Z. Phys. 237, 155-179, 1970.

Wänke, H., H. Kruse, H. Palme, and B. Spettel, Intrumental neutron activation analysis of lunar samples and the identification of primary matter in the lunar highlands, J. Radioanal. Chem. 38, 363-378, 1977.

Wänke, H., Constitution of terrestrial planets, Phil. Trans. R. Soc. Lond. A 303, 287-302, 1981.

Figure Captions

Figure 1. Top view of experimental set-up with inlay of detector shielding. Symbols: A= neutron generator room, B= detector room, C= concrete shielding wall, D= detector with shielding, M= BF_3-monitor for neutrons, N= neutron generator, T= target (placed in window of concrete wall).

Figure 2. Relative efficiency of the used HPGe detector in a log-log plot.

Figure 3a and 3b. Prompt gamma-ray spectrum of an iron target and surrounding material as Ge, Al, Pb, B, paraffin, and concrete. The counts are plotted on logarithmic scale. Symbols: Fe= Fe-56, Al= Al-27, Si= Si-28, O= O-16, a= (n,$\alpha\gamma$), g= (n,γ), n= (n,nγ), 2n= (n,2nγ), s= single escape, d= double escape, Dop= Doppler broadened.

Figure 4. Doppler broadened peaks (sawtooth shape) of germanium neutron-scattering reaction lines and peaks of surrounding material. The counts are plotted on linear scale. Symbols: g= (n,γ), n= (n,nγ), Dop= Doppler broadened.

Figure 5. The 'carbon bump' of a paraffin target and surrounding shielding: Doppler broadening of the $^{12}C(n,n\gamma)$ 4438 keV line. The maximum of the bump is shifted by ca. 15 keV and has a FWHM of 53 keV compared to a FWHM of 4.8 keV of the narrow $^{28}Si(n,\gamma)$ 4423 keV line. The counts are plotted on linear scale. Symbols: g= (n,γ), n= $(n,n\gamma)$, s= single escape peak.

Figure 6. Differential neutron spectrum at target position, normalized to 14 MeV.

Figure 7. Deviation of measured iron gamma-ray flux of neutron-capture reaction lines to values for the capture of thermal neutrons of Stelts and Chrien [1978] in percent.

Foil	Energy	Reaction	Halflife
Au	thermal	$^{197}Au(n,\gamma)^{198}Au$	2.7 d
Au (Cd)	epithermal	$^{197}Au(n,\gamma)^{198}Au$	2.7 d
Al	6-14 MeV	$^{27}Al(n,\alpha)^{24}Na$	15 h
Al	8-14 MeV	$^{27}Al(n,p)^{27}Mg$	9.5 m
Cu	14 MeV	$^{63}Cu(n,2n)^{62}Cu$	9.7 m

Table 1 Foils and reactions used to determine the neutron spectrum.

Target	Composition	Weight [kg]	Depth [g/cm^2]	σ_{th} [b]	Σ [cm^{-1}]
Al	Al 98%, Mg 1%, Si 1%	13.15	2.68	0.23	0.014
Mg	Mg 90%, Al 9%, Zn 1%	21.75	3.12	0.063	0.0025
Fe	Fe 99.9%	53.60	7.87	2.55	0.22
Si	SiO_2 99%	35.70	6.26	0.17	0.0014
Concrete	given in Table 9	168.75	30.0	-	-

Table 2 Composition, weight, depth, and cross section of the targets. (σ_{th}= thermal cross section, Σ= thermal macroscopic cross section).

Energy [keV]	Reaction	Peak Area [counts]	SD %	Flux [γ/cm²min]	SD %
846.7	^{56}Fe(n,nγ)	485231	1.0	1498	39
931.2	^{56}Fe(n,2nγ)	24231	3.6	51	63
1238.3	^{56}Fe(n,nγ)	156220	0.7	440	46
1316.4	^{56}Fe(n,2nγ)	11688	5.5	47	41
1407.7	^{54}Fe(n,nγ)	17133	3.9	69	36
1612.7	^{56}Fe(n,γ)	30355	2.1	283	18
1725.1	^{56}Fe(n,γ)	37697	1.6	321	20
1810.9	^{56}Fe(n,nγ)	21093	5.5	NT	
2112.9	^{56}Fe(n,nγ)	8819	7.7	22	81
2523.1	^{56}Fe(n,nγ)	788 DL		-	
2601.0	^{56}Fe(n,nγ)	784 DL		-	
3601.9	^{56}Fe(n,nγ)	657 DL		-	
3196.3	^{56}Fe(n,γ) d	4728	7.4	83	17
3707.3	^{56}Fe(n,γ) s	4363	7.6	79	22
4218.3	^{56}Fe(n,γ)	8819	3.1	200	16
4898.3	^{56}Fe(n,γ) d	10615	2.5	289	16
5409.3	^{56}Fe(n,γ) s	11825	2.3	351	16
5920.3	^{56}Fe(n,γ)	13053	2.4	407	16
4996.5	^{56}Fe(n,γ) d	11006	2.2	301	16
5507.5	^{56}Fe(n,γ) s	12863	2.2	377	16
6018.5	^{56}Fe(n,γ)	12931	1.8	430	16
6256.8	^{56}Fe(n,γ) d	6128	3.0	247	15
6767.8	^{56}Fe(n,γ) s	7205	3.1	261	17
7278.8	^{56}Fe(n,γ)	5859	2.6	225	17
6609.1	^{56}Fe(n,γ) d	35180	1.3	1237	16
7120.1	^{56}Fe(n,γ) s	41886	1.0	1699	16
7631.1	^{56}Fe(n,γ)	28288	1.1	1271	16
6623.5	^{56}Fe(n,γ) d	30604	1.6	1080	16
7134.5	^{56}Fe(n,γ) s	36370	1.1	1461	16
7645.5	^{56}Fe(n,γ)	24462	1.2	1124	16

Table 3 Iron target: peak area and flux of selected gamma rays. SD = standard deviation: DL = detection limit; NT = no target signal; s, d = single, double escape peak.

Energy [keV]	Reaction	Peak Area [counts]	SD %	Flux [γ/cm^{2}min]	SD %
843.8	^{27}Mg ^{27}Al(n,nγ)	54778	11	80	72
1014.0	^{27}Mg ^{27}Al(n,nγ)	79683	1.2	123	50
1778.8	^{28}Al	156572	0.8	NT	
1808.7	^{27}Al(n,dγ)	20513	5.1	NT	
2981.0	^{27}Al(n,nγ)	655 DL		-	
3004.0	^{27}Al(n,nγ)	680 DL		-	
6702.0	^{27}Al(n,γ) d	3407	4.8	78	20
7213.0	^{27}Al(n,γ) s	4103	3.7	113	18
7724.0	^{27}Al(n,γ)	3106	3.9	94	18

Table 4 Aluminium target: peak area and flux of selected gamma rays. SD = standard deviation; DL = detection limit; NT = no target signal; s, d = single, double escape peak.

Energy [keV]	Reaction	Peak Area [counts]	SD %	Flux [γ/cm^{2}min]	SD %
1273.3	^{28}Si(n,γ)	15865	3.4	NT	
1778.8	^{28}Si(n,nγ) ^{28}Si(n,p)^{28}Al	218458	0.4	552	58
2093.1	^{28}Si(n,γ)	22565	1.8	NT	
2235.4	^{30}Si(n,nγ)	4012	13	13	88
2838.7	^{28}Si(n,nγ)	2434	12	NT	
3200.0	^{28}Si(n,nγ)	682	DL	-	
2517.5	^{28}Si(n,γ) d	11878	3.0	25	89
3028.5	^{28}Si(n,γ) s	12071	2.8	43	83
3539.5	^{28}Si(n,γ)	40655	1.2	117	80
4497.2	^{28}Si(n,nγ)	2043	10	NT	
3912.0	^{28}Si(n,γ) d	14007	6.1	NT	
4423.0	^{28}Si(n,γ) s	15043	2.9	64	65
4934.0	^{28}Si(n,γ)	27372	1.3	117	68
5099.2	^{28}Si(n,nγ)	522	DL	-	
6381.0	^{28}Si(n,γ)	3799	4.9	NT	
5855.7	^{28}Si(n,nγ) d	2622	8.8	NT	
6366.7	^{28}Si(n,nγ) s	3162	5.6	NT	
6877.7	^{28}Si(n,nγ)	2517	6.5	NT	
6178.0	^{28}Si(n,γ) d	2129	7.0	NT	
6689.0	^{28}Si(n,γ) s	2178	7.2	17	75
7200.0	^{28}Si(n,γ)	1956	7.5	NT	

Table 5 Silicon target: peak area and flux of selected gamma rays. SD = standard deviation; DL = detection limit; NT = no target signal; s, d = single, double escape peak.

Energy [keV]	Reaction	Peak Area [counts]	SD %	Flux [γ/cm²min]	SD %
1129.7	$^{26}Mg(n,n\gamma)$	8497	7.1	20	59
1368.6	$^{24}Mg(n,p)^{24}Na$ $^{24}Mg(n,n\gamma)$	76860	1.4	659	17
1808.7	$^{25}Mg(n,\gamma)$ $^{26}Mg(n,n\gamma)$	24260	4.4	123	31
2753.9	$^{24}Mg(n,p)^{24}Na$ $^{24}Mg(n,n\gamma)$	7314	3.7	20	73
2828.5	$^{24}Mg(n,\gamma)$	3559	14	53	21
3867.1	$^{24}Mg(n,n\gamma)$	574 DL		-	
2896.0	$^{24}Mg(n,\gamma)$ d	657 DL		-	
3407.0	$^{24}Mg(n,\gamma)$ s	670 DL		-	
3918.0	$^{24}Mg(n,\gamma)$	2569	13	51	20
4238.0	$^{24}Mg(n,n\gamma)$	621 DL		-	

Table 6 Magnesium target: peak area and flux of selected gamma rays. SD = standard deviation; DL = detection limit; s, d = single, double escape peak.

Element	weight %	σ [b] (n,γ)	Σ [cm^{-1}]
H	0.9*	0.33	$4.8 \cdot 10^{-3}$
C	0.1*	0.0034	$4.8 \cdot 10^{-7}$
O	51.9	0.00027	$1.3 \cdot 10^{-5}$
Mg	0.43	0.063	$1.6 \cdot 10^{-5}$
Al	2.14	0.23	$2.6 \cdot 10^{-4}$
Si	32.8	0.16	$2.7 \cdot 10^{-3}$
Ca	10.0	0.43	$1.6 \cdot 10^{-3}$
Fe	0.846	2.55	$5.6 \cdot 10^{-4}$

Table 7 Composition of concrete target. σ = cross section for (n,γ)-reaction, Σ = macroscopic cross section, * = estimation.

Energy [keV]	Reaction	Relative Flux	SD %
2223.3	$^{1}H(n,\gamma)$	NT	
3854.0	$^{16}O(n,\alpha\gamma)$	0.327	48
5107.4	$^{16}O(n,n\gamma)+^{16}N$ d	1.37	35
5648.4	$^{16}O(n,n\gamma)+^{16}N$ s	2.96	25
6129.4	$^{16}O(n,n\gamma)+^{16}N$	2.10	34
1014.4	$^{27}Al(n,n\gamma)$	NT	
6702.0	$^{27}Al(n,\gamma)$ d	NT	
7213.0	$^{27}Al(n,\gamma)$ s	0.0698	46
7724.0	$^{27}Al(n,\gamma)$	0.0337	70
2517.5	$^{28}Si(n,\gamma)$ d	0.226	37
3028.5	$^{28}Si(n,\gamma)$ s	0.286	33
3539.5	$^{28}Si(n,\gamma)$	0.926	37
3912.0	$^{28}Si(n,\gamma)$ d	0.457	32
4423.0	$^{28}Si(n,\gamma)$ s	0.513	31
4934.0	$^{28}Si(n,\gamma)$	1.00	30
5359.0	$^{28}Si(n,\gamma)$ d	0.116	41
5870.0	$^{28}Si(n,\gamma)$ s	0.227	30
6381.0	$^{28}Si(n,\gamma)$	0.158	38
5855.7	$^{28}Si(n,n\gamma)$ d	0.146	33
6377.7	$^{28}Si(n,n\gamma)$ s	0.178	30
6877.7	$^{28}Si(n,n\gamma)$	0.0952	49
1942.7	$^{40}Ca(n,\gamma)$	0.479	34
3225.6	$^{40}Ca(n,n\gamma)$ s	0.130	20
3736.6	$^{40}Ca(n,n\gamma)$	0.138	39
5398.0	$^{40}Ca(n,\gamma)$ d	0.183	40
5909.0	$^{40}Ca(n,\gamma)$ s	0.350	31
6420.0	$^{40}Ca(n,\gamma)$	0.444	26
1238.3	$^{56}Fe(n,n\gamma)$	NT	
7631.1	$^{56}Fe(n,\gamma)$	NT	
7645.5	$^{56}Fe(n,\gamma)$	NT	

Table 8 Concrete target: peak area and flux of selected gamma rays. SD = standard deviation; DL = detection limit; NT = no target signal; s, d = single, double escape peak.

Element	Energy [keV]	σ [b]	I_γ	I_m	I_c
Al	7724	0.23	0.3	0.03	0.05
Ca	6420	0.43	0.4	0.4	0.4
	1942		0.8	0.4	0.8
Si	6381	0.16	0.13	0.2	0.2
	4934		0.61	≡1	≡1
	3540		0.66	0.9	1.1

Table 9 Comparison of measured (I_m) with calculated (I_c) relative fluxes for (n,γ) lines according to the composition of the concrete target (I_γ= yield of gamma ray per neutron capture [Reedy, 1978]).

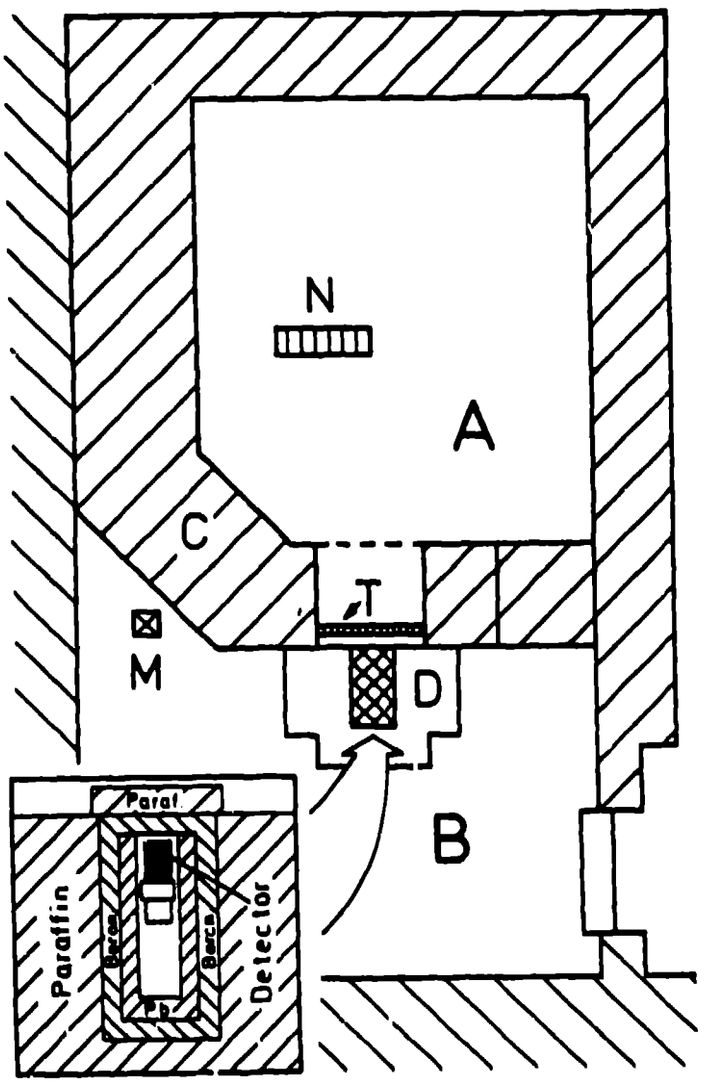

Figure 1

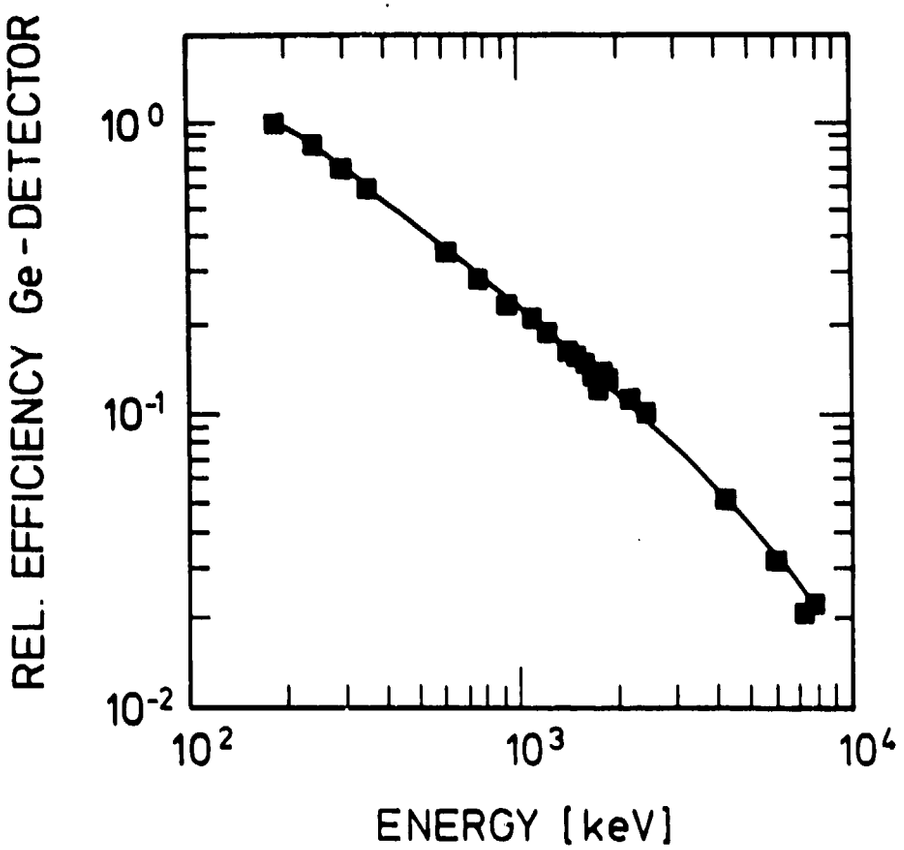
REL. EFFICIENCY Ge-DETECTOR
10 0
10-1
10-2
10 2
10 3
10 4
ENERGY [keV]

Figure 2

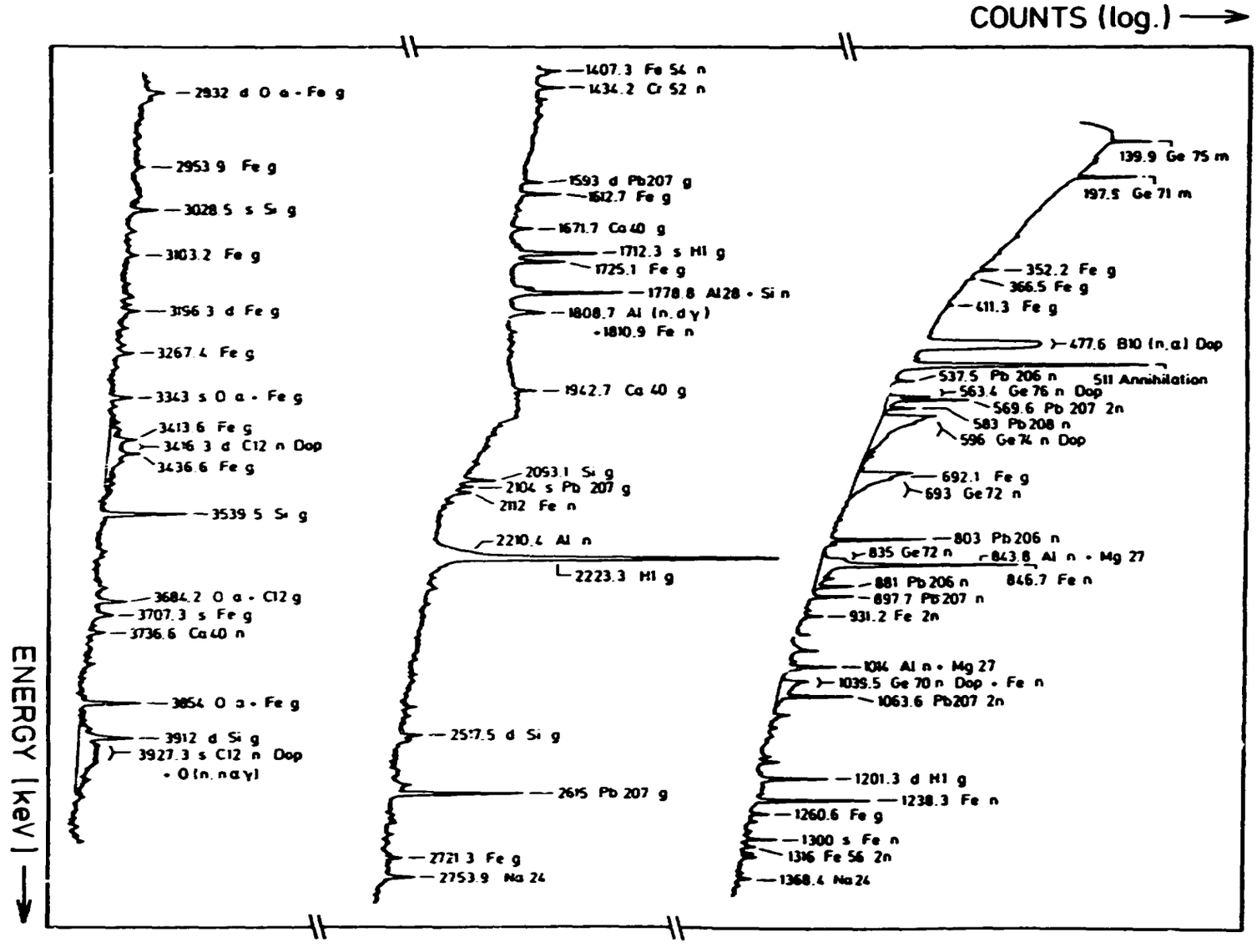
COUNTS (log.) ⟶
ENERGY [keV] ⟶
2832 d O α - Fe g
2953 9 Fe g
3028 5 s Si g
3103.2 Fe g
3156 3 d Fe g
3267 4 Fe g
3343 s O α - Fe g
3413 6 Fe g
3416 3 d C12 n Dop
3436 6 Fe g
3539 5 Si g
3684.2 O α - C12 g
3707.3 s Fe g
3736.6 Ca40 n
3854 O α - Fe g
3912 d Si g
3927.3 s C12 n Dop
- O (n, nαγ)
1407.3 Fe 54 n
1434.2 Cr 52 n
1593 d Pb207 g
1612.7 Fe g
1671.7 Ca40 g
1712.3 s H1 g
1725.1 Fe g
1778.8 Al28 - Si n
1808.7 Al (n, dγ)
- 1810.9 Fe n
1942.7 Ca 40 g
2093.1 Si g
2104 s Pb 207 g
2112 Fe n
2210.4 Al n
2223.3 H1 g
2517.5 d Si g
2615 Pb 207 g
2721 3 Fe g
2753.9 Na 24
139.9 Ge 75 m
197.9 Ge 71 m
352.2 Fe g
366.5 Fe g
411.3 Fe g
477.6 B10 (n, α) Dop
511 Annihilation
537.5 Pb 206 n
563.4 Ge 76 n Dop
569.6 Pb 207 2n
583 Pb 208 n
596 Ge 74 n Dop
692.1 Fe g
693 Ge 72 n
803 Pb 206 n
835 Ge 72 n
843.8 Al n - Mg 27
846.7 Fe n
881 Pb 206 n
897 7 Pb 207 n
931.2 Fe 2n
1014 Al n - Mg 27
1039.5 Ge 70 n Dop - Fe n
1063.6 Pb207 2n
1201.3 d H1 g
1238.3 Fe n
1260.6 Fe g
1300 s Fe n
1316 Fe 56 2n
1368.4 Na24

Figure 3a

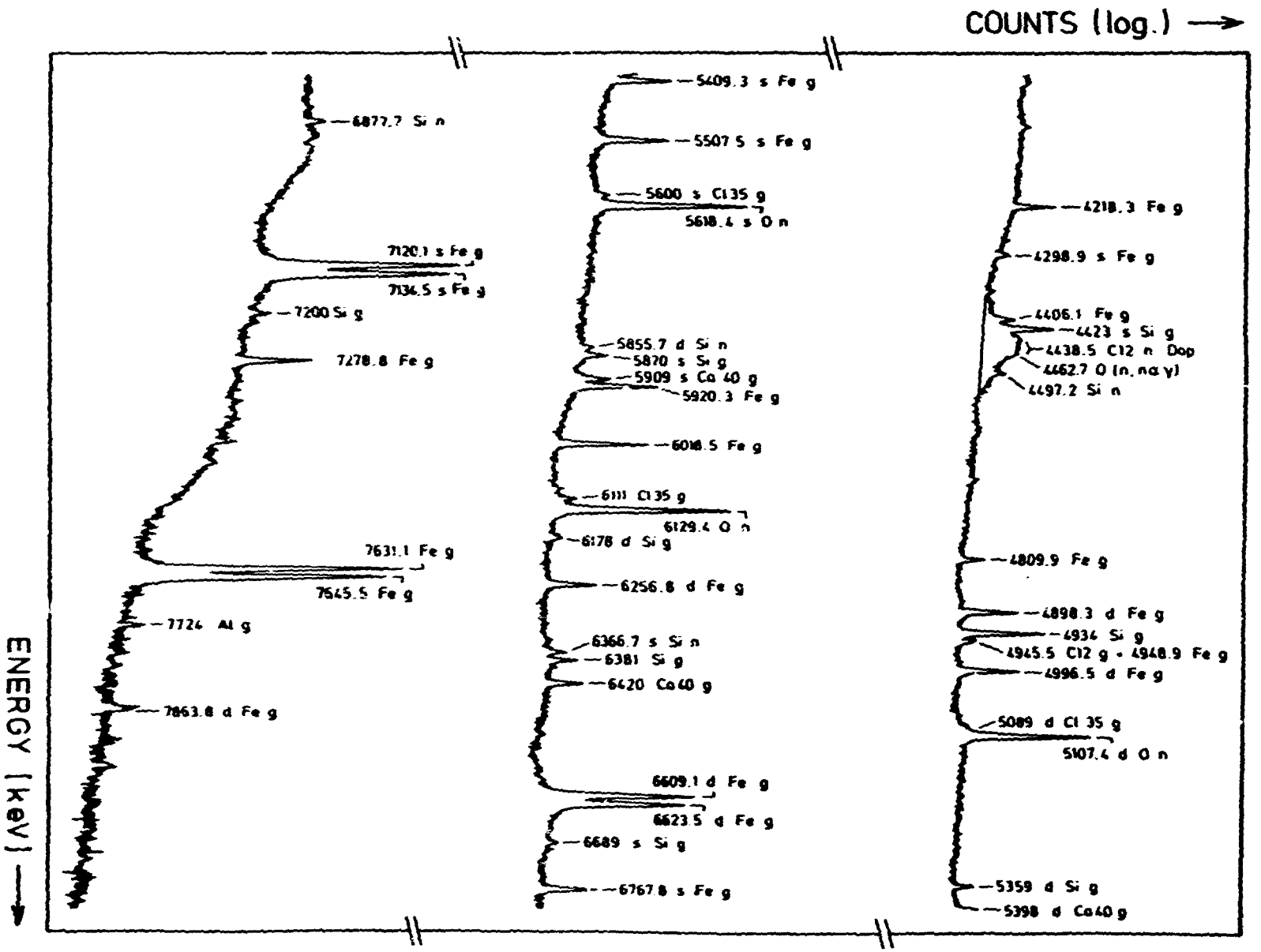
COUNTS (log.) →
ENERGY (keV) →
6877.7 Si n
7120.1 s Fe g
7134.5 s Fe g
7200 Si g
7278.8 Fe g
7631.1 Fe g
7645.5 Fe g
7724 Al g
7863.8 d Fe g
5409.3 s Fe g
5507.5 s Fe g
5600 s Cl35 g
5618.4 s O n
5855.7 d Si n
5870 s Si g
5909 s Ca 40 g
5920.3 Fe g
6018.5 Fe g
6111 Cl35 g
6129.4 O n
6178 d Si g
6256.8 d Fe g
6366.7 s Si n
6381 Si g
6420 Ca40 g
6609.1 d Fe g
6623.5 d Fe g
6689 s Si g
6767.8 s Fe g
4218.3 Fe g
4298.9 s Fe g
4406.1 Fe g
4423 s Si g
4438.5 Cl2 n Dop
4462.7 O (n, nα γ)
4497.2 Si n
4809.9 Fe g
4898.3 d Fe g
4934 Si g
4945.5 Cl2 g + 4948.9 Fe g
4996.5 d Fe g
5089 d Cl 35 g
5107.4 d O n
5359 d Si g
5398 d Ca40 g

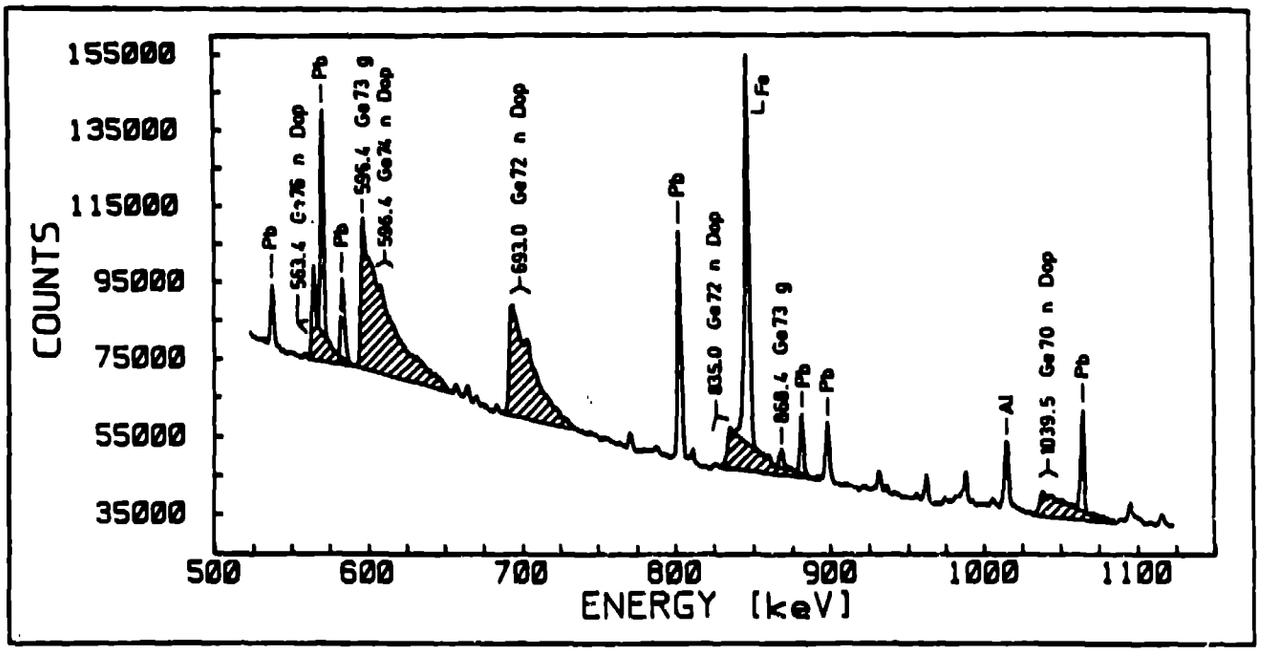
155000
135000
115000
95000
75000
55000
35000
COUNTS
500
600
700
800
900
1000
1100
ENERGY [keV]
Pb
563.4 Ge76 n Dop
Pb
Pb
596.4 Ge73 g
596.4 Ge74 n Dop
691.0 Ge72 n Dop
Pb
835.0 Ge72 n Dop
Fe
868.4 Ge73 g
Pb
Pb
Al
1039.5 Ge70 n Dop
Pb

Figure 4

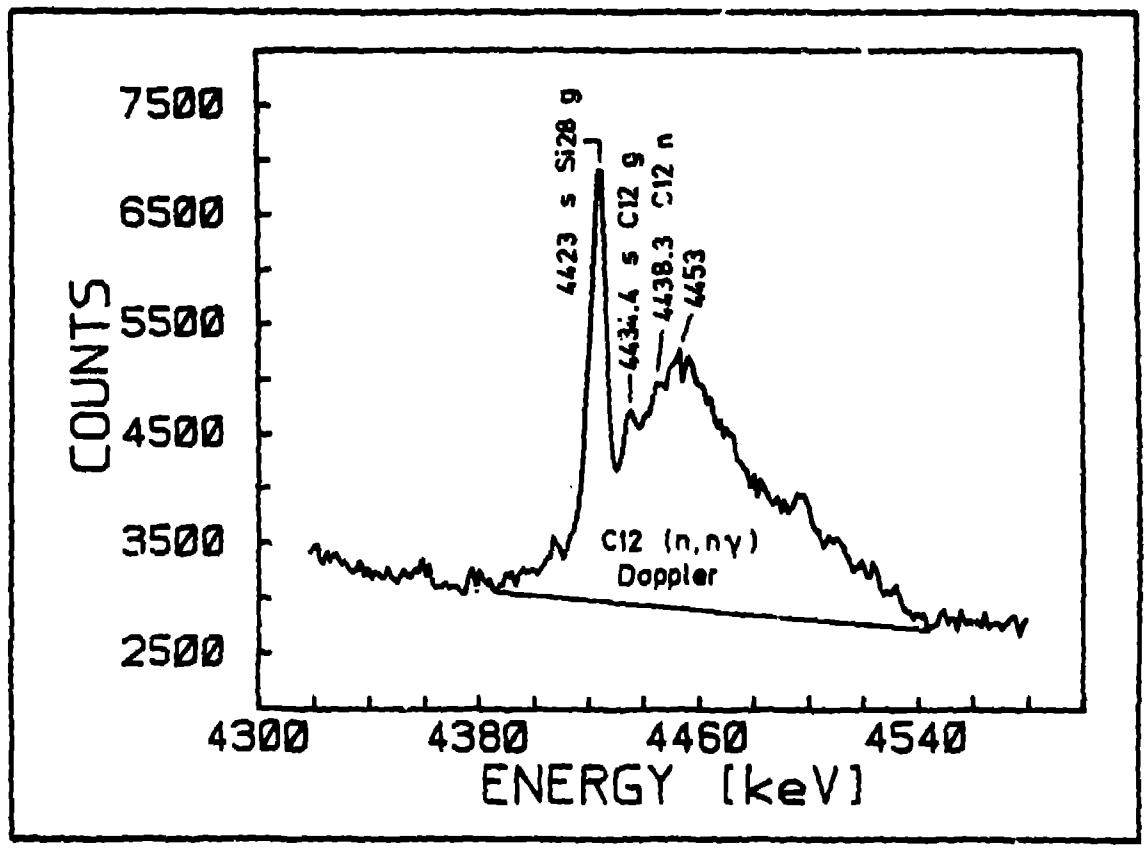
7500
6500
5500
4500
3500
2500
COUNTS
4423 s Si28 g
4434.4 s C12 g
4438.3 C12 n
4453
C12 (n,nγ)
Doppler
4300
4380
4460
4540
ENERGY [keV]

Figure 5

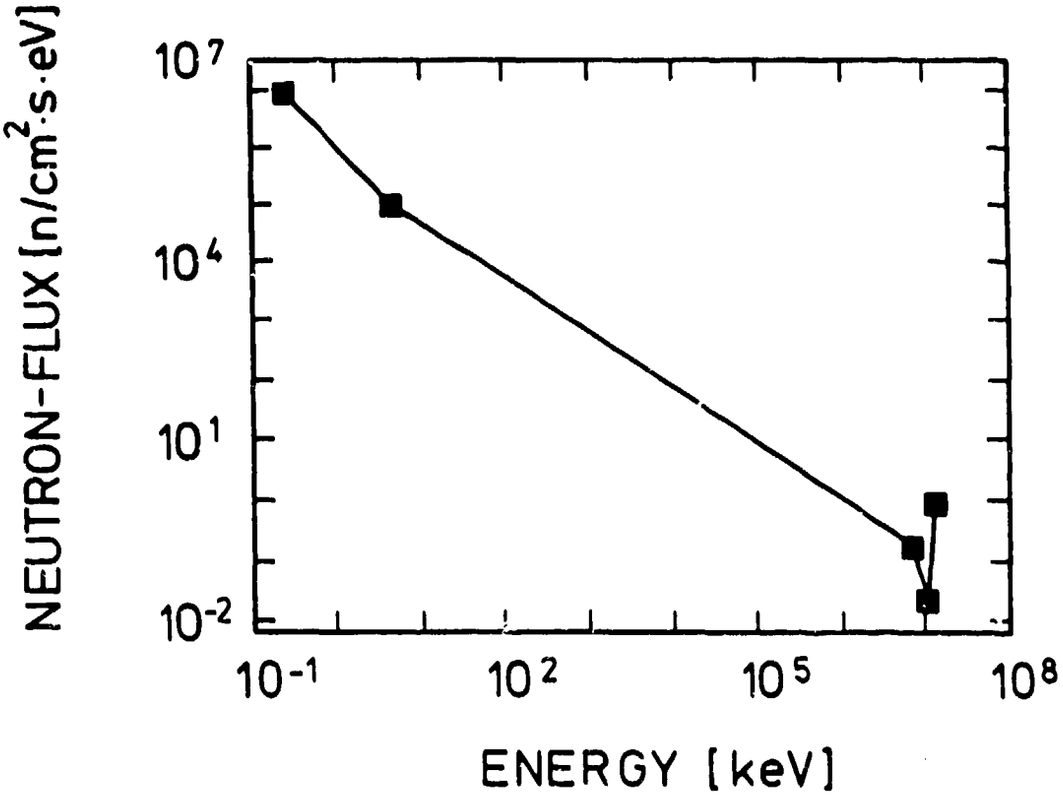
NEUTRON-FLUX [n/cm²·s·eV]
10⁷
10⁴
10¹
10⁻²
10⁻¹
10²
10⁵
10⁸
ENERGY [keV]

Figure 6

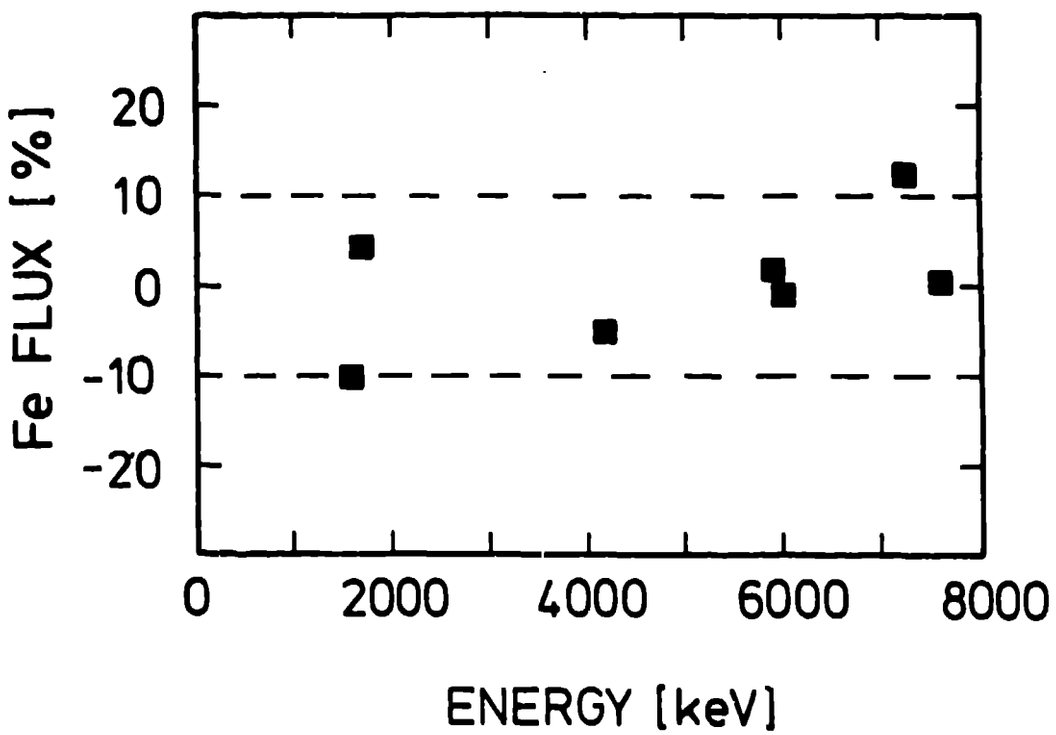

Figure 7